Maneuvering drone noise investigation in a reverberant environmenta)

Zamponi, R.; Gioli Torrione, G.; Zůbek, V.; Gallo, E.; Zarri, A.; Schram, C.

DOI
10.1121/10.0036900

Publication date
2025

Document Version
Final published version

Published in
Journal of the Acoustical Society of America

JUNE 18 2025

Maneuvering drone noise investigation in a reverberant environment[a)]

R. Zamponi ; G. Gioli Torrione; V. Zůbek ; E. Gallo ; A. Zarri ; C. Schram

J. Acoust. Soc. Am. 157, 4468–4481 (2025)
https://doi.org/10.1121/10.0036900

JASA ARTICLE

Maneuvering drone noise investigation in a reverberant environment[a)]

R. Zamponi,[1,2,b)] G. Gioli Torrione,[1] V. Zůbek,[1,3] E. Gallo,[1] A. Zarri,[1] and C. Schram[1]

[1]*Department of Environmental and Applied Fluid Dynamics, von Karman Institute for Fluid Dynamics, Waterloosesteenweg 72, B-1640 Sint-Genesius-Rode, Belgium*

[2]*Department of Flow Physics and Technology, Delft University of Technology, Kluyverweg 1, 2629 HS Delft, The Netherlands*

[3]*Department of Aviation Technology, University of Defence, Kounicova 65, 662 10 Brno-střed, Czech Republic*

ABSTRACT:

With the rapid proliferation of unmanned aerial vehicles, understanding the aeroacoustics of drones in operating conditions is essential to mitigate perceived annoyance. Performing these measurements in a large indoor test hall is particularly attractive, as it allows the execution of complex drone maneuvers under controlled atmospheric conditions, with high-precision trajectory tracking provided by motion capture systems. Yet, not being acoustically treated, these facilities present challenging reverberant conditions for acoustic measurements. This research work focuses on investigating a maneuvering quadcopter drone inside an indoor test hall and proposes a methodology based on phased-array techniques to decontaminate the recorded noise from the reverberation effects using a tailored Green's function. The results indicate that the tonal contributions of the noise spectrum are significantly influenced by drone operation and orientation, with distinct changes in the blade pass frequencies linked to the varying speeds of the front and back rotors during different flight phases. By filtering out spurious broadband noise due to sound reflections, the proposed dereverberation methodology facilitates the tracking of these tonal components, which can be more clearly visualized in the noise spectrum. The study eventually highlights the importance of analyzing the drone trajectory when interpreting the corresponding noise radiation.

 https://doi.org/10.1121/10.0036900

(Received 12 February 2025; revised 15 May 2025; accepted 3 June 2025; published online 18 June 2025)

[Editor: Eric Greenwood] Pages: 4468–4481

I. INTRODUCTION

The social acceptance of unmanned aerial vehicles (UAVs) represents a major challenge (Schäffer *et al.*, 2021; Sabatini and Gardi, 2023), despite the benefits that should result in diverse applications (Rizzi *et al.*, 2020). Whether for industry or public services, the advantages of drones are multiple (Gupta *et al.*, 2021). For example, they have the potential to provide a significant contribution to medical care as a fast and safe option in the event of an urgent need for supplies, such as drugs or biological materials. In this regard, the success rate of transplants is aided by the ability of the UAV to avoid urban traffic and safely deliver payloads in a short time (Scalea *et al.*, 2018). Another notable example is their use at remote sites: inspection of high-rise structures during maintenance operations poses significant risks to humans, and drones can play this crucial role (Falorca *et al.*, 2021). For example, the deployment of drone swarms equipped with remote sensing devices for acoustic measurements represents an alternative solution to monitoring the structural health of offshore wind turbines (Poozesh *et al.*, 2017; Shafiee *et al.*, 2021). Likewise, drone package delivery can help reduce traffic congestion and carbon emissions in densely populated areas (Kellermann *et al.*, 2020). Nevertheless, the perceived noise of these vehicles remains an obstacle to their social acceptance (Schäffer *et al.*, 2021).

Drone annoyance is a complex and relatively recent research topic (Gwak *et al.*, 2020; Torija *et al.*, 2019; Yupa-Villanueva *et al.*, 2024). The noise generation mechanisms associated with these vehicles include periodic mutual interactions between the propellers and the airframe that cause tonal noise on the one hand (Roger and Moreau, 2020; Zarri *et al.*, 2022) and aperiodic mechanisms that induce broadband noise on the other hand (Kim *et al.*, 2019; Whelchel *et al.*, 2022). The relative importance of the tonal and broadband components, which can also exhibit fast temporal modulations, yields a drone noise signature that is quite atypical, very noticeable in most acoustic landscapes, and is often pointed out as fairly annoying (Torija and Nicholls, 2022). Even in steady hovering conditions, the continuous adjustment of the propeller rotational speeds by the flight control system trying to maintain vehicle stability in gusty atmospheric conditions causes a time-varying high-pitched, persistent, and irritating buzz. Outdoor tests of hovering UAVs have established that, at equivalent loudness levels, drones are more annoying than civil aircraft (Gwak *et al.*, 2020). Quite logically, more aggressive maneuvers, such as the fast

[a)]This paper is part of a special issue on Advanced Air Mobility Noise: Predictions, Measurements, and Perception.

[b)]Email: riccardo.zamponi@vki.ac.be

https://doi.org/10.1121/10.0036900

transition from hovering to forward flight, deceleration, descent, etc., are also perceived as disturbing (Ramos-Romero *et al.*, 2023; Green *et al.*, 2024).

Studies focused on maneuvering noise remain relatively scarce (Schäffer *et al.*, 2021), compared to hovering and forward translation noise (Intaratep *et al.*, 2016; Sarikaya *et al.*, 2024). Yupa-Villanueva *et al.* (2024) investigated the instantaneous psychoacoustic annoyance (PA) (Torija and Nicholls, 2022) of different UAV models executing outdoor flyover maneuvers. The annoyance was found to be related to the varying speed of most of the drone models tested, with peaks associated with higher speeds. The PA values of several hover, flyover, takeoff, and landing flight procedures were evaluated in the work of Torija Martinez *et al.* (2024).

The aforementioned experimental studies were conducted outdoors. Although open-field tests are more representative of the actual operation of a drone, they can be hindered by uncontrolled atmospheric disturbances, which causes repeatability problems (Naz *et al.*, 2020; Gallo *et al.*, 2022). Fixed-drone measurements offer much better repeatability but exhibit sharper and more intense tones than if a flight controller was actually stabilizing the drone attitude. Maneuvers are, of course, prohibited in this case. Alternatively, UAV noise can be investigated in anechoic environments with microphones and acoustic cameras for hovering or forward-flight conditions (Alkmim *et al.*, 2022; Zhou *et al.*, 2022). The recently proposed ISO 5305 (ISO 5305:2024, 2024) provides requirements and extensive guidelines for measurements in anechoic chambers, as well as in an acoustic wind tunnel and in the free atmosphere. However, the space and availability requirements posed in anechoic testing environments are typically demanding, even for stationary UAV measurements, and are extremely difficult to meet for free-flight maneuvers.

In this paper, an alternative approach is explored, making use of a large indoor test hall, such as the ID2Move facility in Nivelles, Belgium, which allows a wide range of maneuvers of a UAV under flight conditions free from uncontrolled mean wind or gusts. However, not being treated acoustically, the test hall offers challenging reverberant conditions for acoustic measurements, with spurious reflections (Cavanaugh *et al.*, 2010; Savioja and Svensson, 2015) and extended decay times (Waterhouse, 1958) with respect to free-field conditions. The main objective of the present work is to develop an experimental protocol enabling free-field equivalent UAV noise measurements to be taken in reverberant environments and allowing a reliable assessment of the acoustic footprint of these vehicles under operating conditions.

Another issue when measuring drone noise with fixed microphones is the need to compensate for variations in the distance between the noise source and the microphones during a maneuver, in order to obtain a characterization of the noise emissions that is intrinsic to the drone. This requires knowing the position of the drone with sufficient accuracy. Previous studies (Herold and Sarradj, 2024, 2023; Guo *et al.*, 2020; Blanchard *et al.*, 2020) used one or more planar microphone arrays to obtain the trajectory of the drone. This approach provides a source position with a precision that depends on the acoustic wavelength selected for the analysis, usually on the order of a dozen centimeters, using state-of-the-art beamforming algorithms. In the present study, an imaging system based on motion capture cameras and advanced processing algorithms are used to locate the drone with an accuracy on the order of a millimeter. A phased array of microphones is still employed, though with the goal of decontaminating acoustic measurements from the effects of acoustic reflections, knowing the source position thanks to the motion capture system. The proposed decontamination methodology, based on the method of images (Allen and Berkley, 1979; Aretz *et al.*, 2014), makes it possible to access the benefits of an indoor test zone, which allows controlled atmospheric conditions and precise tracking of the drone location, while ensuring that measurements remain unaffected by sound reflections.

The development of these tools and experimental procedures is detailed in Sec. II, together with a presentation of the drone testing facility and the motion capture system. The results provided in Sec. III highlight the effectiveness of the noise decontamination methods and provide a database of noise emissions associated with different standard maneuvers. Conclusions are drawn in Sec. IV.

II. MATERIALS AND METHODS

A. Indoor test hall, instrumentation, and drone model

The ID2Move indoor test hall is illustrated in Fig. 1(a). It offers a spacious environment suitable for maneuvering UAV investigations while avoiding contamination from outdoor atmospheric effects. The dimensions of the room ($23.6 \times 26.8 \times 8.5\,\mathrm{m}^3$) are visible in Fig. 1(b), as well as the reference system considered to present the results. In particular, the z axis is oriented out-of-plane to form a right-handed coordinate system.

A sub-volume of the room is equipped with a Qualisys motion capture system (Qualisys AB, Göteborg, Sweden) composed of 12 Arqus A5 high-speed cameras (Qualisys AB, Göteborg, Sweden) with a frame rate up to 700 Hz. The maximum capture distance is 26 m, and the spatial resolution obtained in the tests was on the order of a millimeter. The recording and processing of the UAV trajectory is performed through the Qualisys Track Manager software (Qualisys AB, Göteborg, Sweden).

The acoustic characterization of the test hall is achieved using a monopolar source obtained by plugging a loudspeaker housing box into a hose pipe with an internal diameter of about 2 cm. The loudspeaker is a Monacor model SPH-75/8 (Monacor International, Bremen, Germany) and is driven by a JBL UREI 6230 power amplifier (JBL, Los Angeles, CA), taking as input a logarithmic chirp signal sweeping from 100 Hz to 10 kHz over a duration of 5 s that is produced by an Agilent 33120 A signal generator (Keysight Technologies, Santa Rosa, CA). The monopolar far-field directivity of the hose outlet has been verified in the

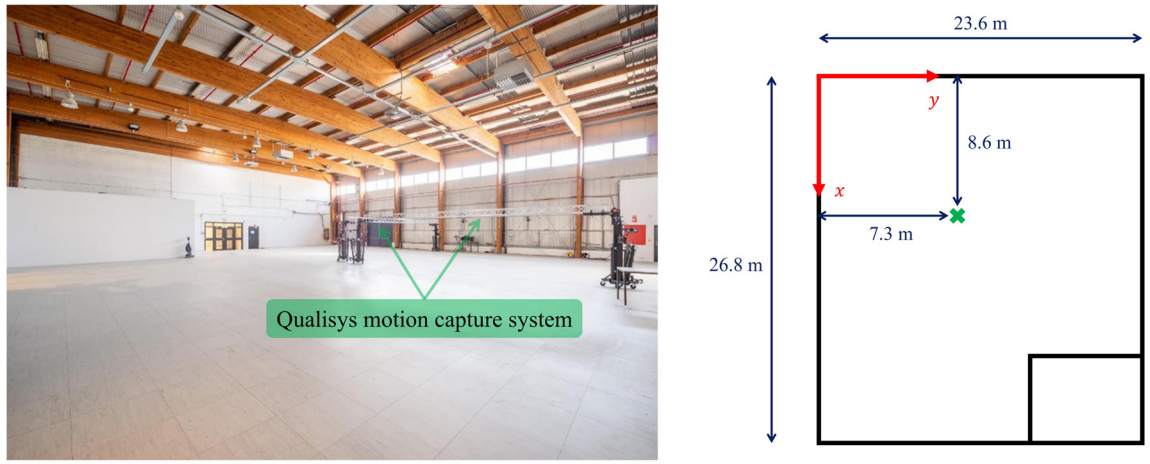

FIG. 1. (A) ID2Move indoor test hall for the UAV aeroacoustic investigation, equipped with the Qualisys motion capture system. Adapted from ID2Move (2015). Copyright 2025. (B) Plant of the test hall and reference system considered for presenting the results. The green cross denotes the position of the monopolar sources generated for the acoustic characterization of the room. An enclosed space where the testing equipment is stored is situated in the bottom right corner of the plant.

JAFAAR anechoic chamber of the von Karman Institute for Fluid Dynamics (VKI) (Zamponi *et al.*, 2020), showing deviations of less than ± 0.5 dB for frequencies up to 10 kHz. The source is then located at $x = 8.6$ m and $y = 7.3$ m of lateral distances from the walls of the test hall [see Fig. 1(B)], at varying heights above the floor.

Two microphones are placed at distances of 1 and 0.1 m from the monopolar source and a height of 1 m from the floor to characterize the reverberation effects of the test room. The closest sensor enables normalization of the monopolar source strength. Both microphones are GRAS 40PL-10 free-field type (GRAS Sound & Vibration, Holte, Denmark) with integrated constant-current power amplifier featuring a flat frequency response within ± 1 dB from 50 Hz to 5 kHz and within ± 2 dB from 5 to 20 kHz. They are calibrated in amplitude using a GRAS 42AG piston-phone (GRAS Sound & Vibration, Holte, Denmark) producing a sinusoidal wave of 94 dB at 1 kHz. The acquisition system consists of an NI PXIe-1075 chassis (National Instruments, Austin, TX) controlled by an NI PXIe-8105 dual core embedded controller (National Instruments, Austin, TX).

In addition, a microphone array comprising of 64 capacitor-based microphones model FG23327-P07 (Knowles, Itasca, IL), with a flat frequency response within ± 3 dB for frequencies ranging from 100 Hz to 10 kHz, is used to acquire the noise emitted by the drone. The structure of the array is made of three-dimensional printed resin, with an aperture of approximately 1.5 m. Figure 2(A) shows a photo of the microphone array, while its response expressed by the point-spread function (PSF) (Allen *et al.*, 2002) is illustrated in Fig. 2(B) for a synthetic point source placed at a distance of 1 m and emitting white noise at a frequency of $f = 1$ kHz. The transducers, which are inserted into brass tubes anchored in resin and arranged to form a Dougherty-array disposition (Dougherty, 1998), are connected to the NI PXIe-8105 controller (National Instruments, Austin, TX) through in-house amplifiers and calibrated in amplitude and phase using the semi-empirical method proposed by Moriaux *et al.* (2024). The central microphone is

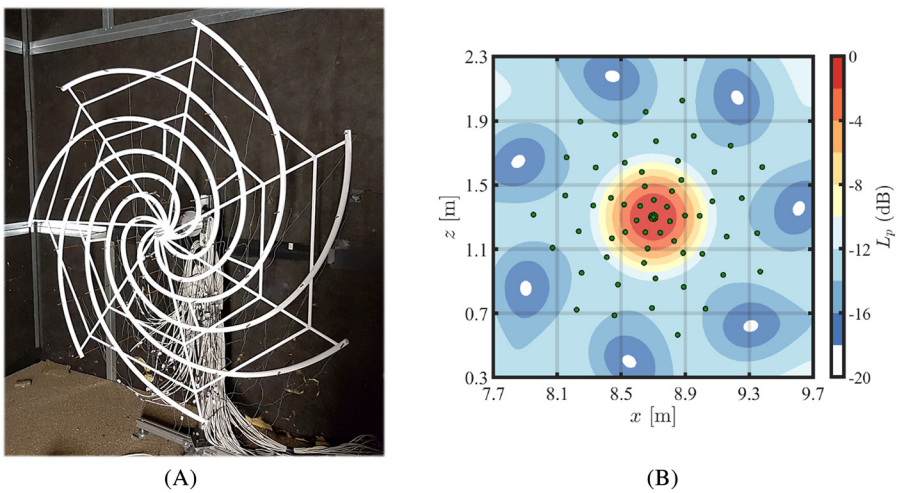

FIG. 2. (A) Dougherty microphone array used for the acoustic measurements. Reproduced with permission from Zamponi *et al.*, in *25th AIAA/CEAS Aeroacoustics Conference* (2019). Copyright 2019 (Zamponi *et al.*, 2019). (B) PSF computed at $f = 1$ kHz for a simulated source emitting white noise at a distance of 1 m from the array.

https://doi.org/10.1121/10.0036900

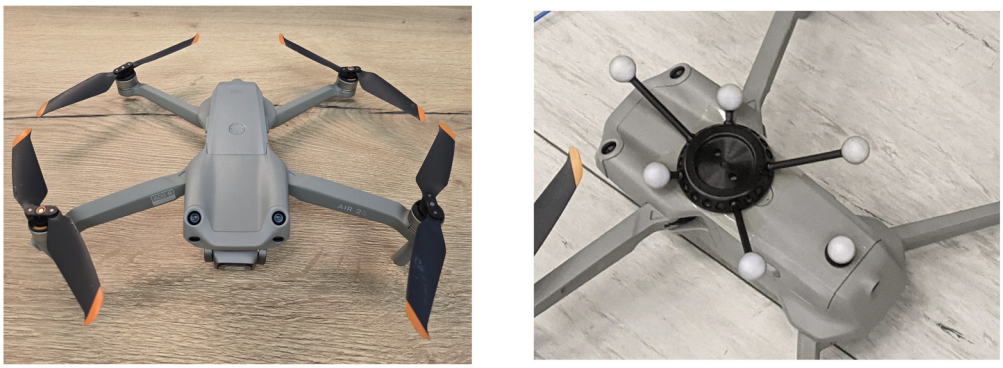

(A) (B)

FIG. 3. (A) DJI Air 2S quadcopter drone investigated in the experiments. (B) Detail of the reflective markers installed on the drone to track its trajectory.

located at $x = 8.7$ m, $y = 6.5$ m, and $z = 1.3$ m with respect to the reference system indicated in Fig. 1(B).

Data are acquired with a sampling frequency of 51.2 kHz and processed using Welch's method (Welch, 1967), with blocks of 2^{12} samples windowed through a Hamming weighting function having a 50% data overlap, thus providing a frequency resolution of 12.5 Hz. The duration of acquisition for the room acoustic characterization is set to 30 s, i.e., corresponding to six full chirp signals, while that for the UAV is variable and depends on the maneuver investigated.

The UAV used during the measurement campaign is the DJI Air 2S (DJI Sky City, Shenzhen, China) commercial drone, a small quadcopter with foldable 7238 low-noise propellers (0.183 m in diameter and 0.097 m of thread pitch) and structure that is depicted in Fig. 3(A). Once they unfold, the front and back pairs of propellers lie in two different horizontal planes. In addition, the center of gravity of the drone is not exactly at the mid-distance between the front and aft propeller pairs. This implies that, in steady hovering conditions, the two pairs of propellers spin at different rotational speeds.

The position and attitude of the drone can be tracked using reflective markers placed on the frame [see Fig. 3(B)], detectable by the motion capture system. A reflective marker is also placed in the vicinity of the central microphone of the array to determine the relative distance between the drone and the array at every time instant. Furthermore, to synchronize the microphones and the camera recordings, a pole topped with an additional marker is struck against the ground after the acquisition starts, thus providing a sharp impulsive sound recorded by the array and a distinct movement detected by the motion capture system.

An overview of the maneuvers performed in this study is provided in Fig. 4. In forward flights, the drone flies in front of the microphone array along the x axis, keeping the y and z coordinates approximately constant. It moves from left to right while accelerating in Fig. 4(A), moves from right to left while decelerating in Fig. 4(B), and performs a side-to-side maneuver from left to right first and from right to left afterward in Fig. 4(C). In the first two maneuvers, the drone is oriented sideways with respect to the microphone array, whereas, in the last one, it faces it. In vertical flights, the drone flies along the z axis, keeping its x and y coordinates. It ascends in Fig. 4(D) and descends in Fig. 4(E), and, in both cases, it faces the microphone array.

B. Characterization of the reverberation effects

As mentioned in Sec. I, the main challenge of performing acoustic measurements of a UAV under operative conditions inside a test hall is represented by the reverberation effects. The sound waves reflected by the room walls interfere (destructively or constructively) with the noise radiated by the drone and affect the sound decay. The methodology required to assess the acoustic field in the ID2Move facility is outlined in this section.

A first characterization of the reverberant conditions of the room can be performed by estimating the reverberation radius, or critical distance, D_c, i.e., the distance from a sound source where the direct sound is equal in strength to the reverberant one. If a spherical wavefront is assumed in the acoustic far field, the latter quantity can be determined by measuring the sound level L_D evaluated in the near field and the sound level L_R evaluated in the far field according to the relation (Davis *et al.*, 2013)

$$D_c = D_{\text{ref}}\, 10^{(L_D - L_R)/20}, \tag{1}$$

with D_{ref} being the reference distance from the source at which L_D is measured. Here, the near field is defined as the region in which the spreading of the acoustic wavefront is not yet spherical. For the ID2Move facility, it results that $D_c \approx 2.2$ m.

Furthermore, the method of images makes it possible to compute the tailored Green's function associated with rigid reflective walls for a given acoustic point source and listener location and a specific frequency (Allen and Berkley, 1979). It consists of introducing a fictional (or image) source to model the reflection of a physical one by the wall, the two sources having the same strength and being symmetric with respect to the wall plane. In the general case in which six walls are present, i.e., in a rectangular room, each image will be itself imaged, providing a higher-order reflection.

Let the vectors $\boldsymbol{x_s} = [x_s, y_s, z_s]$ and $\boldsymbol{x_r} = [x_r, y_r, z_r]$ represent the Cartesian coordinates of a monopolar source and an omnidirectional receiver with respect to the origin of the

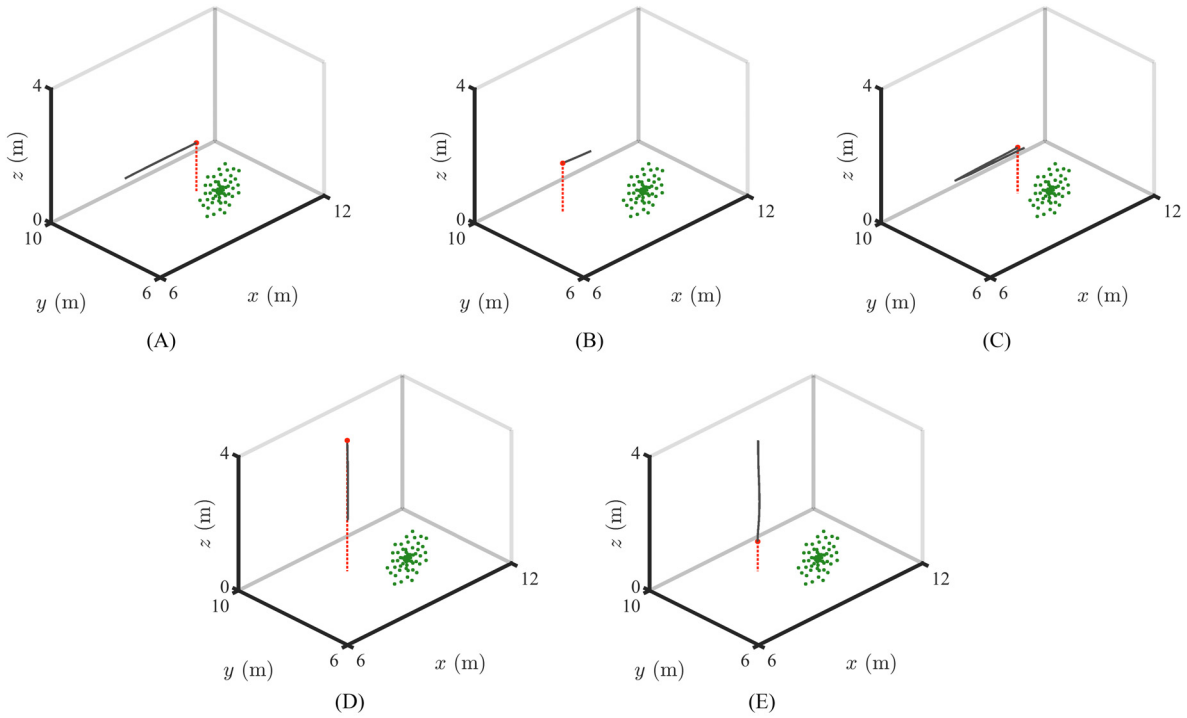

FIG. 4. Trajectories (in black) performed for the investigation of the UAV noise according to the reference system in Fig. 1(B). (A) Forward flight with drone accelerating, (B) forward flight with drone decelerating, (C) drone moving side-to-side, (D) vertical flight with drone ascending, (E) vertical flight with drone descending. The microphones are depicted in green, whereas the UAV position at the end of the maneuver, as well as its projection on the floor, is in red.

reference system, respectively. The vector pointing from every image source to the listener can be defined as

$$\boldsymbol{R}_{\boldsymbol{p},\boldsymbol{q}} = \begin{bmatrix} x_r - x_s + 2\,p_x\,x_s - 2\,q_x\,L_x \\ y_r - y_s + 2\,p_y\,y_s - 2\,q_y\,L_y \\ z_r - z_s + 2\,p_z\,z_s - 2\,q_z\,L_z \end{bmatrix}, \tag{2}$$

where $\boldsymbol{p} = [p_x, p_y, p_z]$ is an integer vector triplet that determines with respect to which wall of the room the image source is reflected and $\boldsymbol{q} = [q_x, q_y, q_z]$ indicates the order of the reflections that are considered. The elements of the former vector can take values of 0 and 1, resulting in a set $\mathcal{P}$ of eight possible permutations. Those of the latter vector can range between $-N_r$ and N_r, N_r being the highest order of reflections imposed in the model to limit the computational complexity, which implies a total of $(2N_r + 1)^3$ combinations for the set $\mathcal{Q}$. L_x, L_y, and L_z represent the length, width, and height of the rectangular room, respectively.

Using the information on the image position and order, the tailored Green's function of the room g_t for a monopolar source is obtained by summing the free-field Green's function of the corresponding physical source, denoted by $\boldsymbol{q} = \boldsymbol{0}$, with those of the different images:

$$g_t(k, \boldsymbol{x_s}, \boldsymbol{x_r}, N_r) = \sum_{\boldsymbol{p}\in\mathcal{P}} \sum_{\boldsymbol{q}\in\mathcal{Q}} \frac{e^{-ik||\boldsymbol{R}_{\boldsymbol{p},\boldsymbol{q}}||}}{4\pi||\boldsymbol{R}_{\boldsymbol{p},\boldsymbol{q}}||}, \tag{3}$$

where k is the acoustic wave number and i is the imaginary unit.

Equation (3) is derived for rigid walls, i.e., without accounting for losses. In practice, this hypothesis is typically invalid and the solution in terms of point image sources may no longer be exact. One approximate way to account for non-rigid walls in the tailored Green's function is by multiplying the second term in the right-hand side of Eq. (3) to the angle-independent reflection coefficient β, resulting in

$$g_t(k, \boldsymbol{x_s}, \boldsymbol{x_r}, N_r) = \sum_{\boldsymbol{p}\in\mathcal{P}} \sum_{\boldsymbol{q}\in\mathcal{Q}} \beta(\boldsymbol{p}, \boldsymbol{q}) \frac{e^{-ik||\boldsymbol{R}_{\boldsymbol{p},\boldsymbol{q}}||}}{4\pi||\boldsymbol{R}_{\boldsymbol{p},\boldsymbol{q}}||}. \tag{4}$$

From a physical perspective, β denotes the percentage of acoustic energy that is actually reflected by a given surface and is linked to the Sabine energy-absorption coefficient, α_a, by the relationship (Allen and Berkley, 1979)

$$\alpha_a = 1 - \beta^2. \tag{5}$$

Since the reflection coefficient is based on the acoustic properties of the materials used for the walls of the room, it is possible to express it as $\beta = \beta_{x_1}^{|q_x - p_x|}\beta_{x_2}^{|q_x|}\beta_{y_1}^{|q_y - p_y|}\beta_{y_2}^{|q_y|}\beta_{z_1}^{|q_z - p_z|}\beta_{z_2}^{|q_z|}$ (Xu *et al.*, 2024), where the subscripts a_1 and a_2, with $a \in \{x, y, z\}$, correspond to the boundaries at $a = 0$ and $a = L_a$, respectively. An overview of the coefficients β_a adopted for the ID2Move facility is given in the Appendix. For frequencies ranging from 0.1 to 5 kHz, for wall-reflection coefficients greater than 0.7, and when both the source and receiver are not too close to the walls, this approach is expected to provide a suitable representation of the tailored Green's function for a realistic rectangular room (Allen and Berkley, 1979). In this work, the method of images has been implemented in an automatic routine that determines g_t and provides the simulated acoustic response

https://doi.org/10.1121/10.0036900

of a given geometry of the room. The image sources are computed up to the order 10.

The suitability of the approach outlined above to characterize constructive and destructive interference patterns of sound reflections can be assessed by comparing g_t with the experimental transfer function (TF) of the ID2Move facility. This quantity relates the reverberant environment and the corresponding anechoic conditions for an acoustic point source, i.e., the loudspeaker described in Sec. II A, placed at the same distance and is calculated according to

$$\mathrm{TF} = 10\,\log_{10}\left(\frac{S_{pp,\mathrm{rev}}}{S_{pp,\mathrm{an}}}\right), \tag{6}$$

with S_{pp} being the power of the acoustic signal $p(t)$ recorded by the microphone. The comparison will be discussed in Sec. III A.

C. Drone-tracking beamforming

The decontamination of the acoustic signals acquired in the test hall from reverberation effects, i.e., their dereverberation, can be performed using phased-array techniques. Acoustic beamforming methods on a moving source usually require a time domain approach, e.g., the rotating source identifier algorithm (Amoiridis *et al.*, 2022), to account for Doppler frequency shift and amplification. Unfortunately, these methods are time-consuming and typically unsuitable for corrective approaches. The purpose of this section is to present the assumptions under which frequency-domain beamforming can be applied to moving sources, i.e., to track the drone trajectory. The proposed approach will be referred to as *drone-tracking beamforming*.

Consider a moving monopolar source with strength Q, at a position $\boldsymbol{x}_s$, and with a retarded time τ. The acoustic pressure seen by the microphone at a position $\boldsymbol{x}_r$ and receiver time $t = \tau + ||\boldsymbol{x}_r - \boldsymbol{x}_s||/c_0$ in free-field conditions, c_0 being the speed of sound, is described by

$$p(\boldsymbol{x}_r, f) = \frac{Q}{4\pi||\boldsymbol{x}_r - \boldsymbol{x}_s||} e^{-ikc_0\,(t-||\boldsymbol{x}_r-\boldsymbol{x}_s||/c_0)}, \tag{7}$$

where the Doppler amplitude and frequency modulations have been neglected, considering the low displacement velocity of the drone operated in this study. The time signal is now divided into short overlapping chunks such that the change in source position during each time segment is negligible. The same parameters for Welch's method mentioned in Sec. II A are used to define the duration of the time chunks, i.e., 0.08 s with 50% of overlap. This ensures an adequate trade-off between accurately estimating the signal power in the frequency range of interest and granting a negligible source displacement.

The pressure data from Eq. (7) for every time segment are then processed through a conventional frequency-domain beamforming algorithm (Allen *et al.*, 2002; Zamponi, 2021). The reverberation effects in the test hall are accounted for by including the tailored Green's function in Eq. (4) in the steering-vector formulation, which refers to a monopolar source. The corresponding beamforming output A_j related to the j-th point of the considered scan grid is given by

$$A_j = \boldsymbol{w}_j^*\,\boldsymbol{C}\,\boldsymbol{w}_j, \tag{8}$$

where $\boldsymbol{w}_j = \boldsymbol{g}_j/||\boldsymbol{g}_j||^2$ is the normalized steering vector, $\boldsymbol{g}_j$, containing the tailored Green's functions g_t between each microphone and the j-th grid point, $\boldsymbol{C}$ is the cross-spectral matrix of the recorded signals, and the operator * denotes the Hermitian transpose.

It is important to stress that, in sound source localization, there is no reason for the scan grid to perfectly match the true physical source region, which can be identified as the minimum region characterized by finite acoustic power. The potential sources in the scan grid, which are assumed to be uncorrelated monopoles, are indeed considered *equivalent sources* having the same acoustic power as the physical source region. The tailored Green's function in Eq. (4), calculated using the method of images and derived for a point monopole, cannot be directly used to model the sound radiated by the drone, i.e., the physical source, most likely characterized by a more complex directivity pattern. However, it can be used to compute the sound emitted by each of these equivalent sources in the test hall. In doing so, the sound field reconstructed by the beamforming method describes the acoustic signature of the UAV effectively decontaminated from reverberation effects.

Subsequently, the source strength from the sound map in Eq. (8) can be integrated within a predefined region of integration (ROI) to determine the noise levels radiated by the drone using the source power integration (SPI) method (Merino-Martínez *et al.*, 2020). This technique is based on the assumption that the integrated source power can be represented by a synthetic acoustic monopole, which is typically located at the center of the ROI and thus needs to be appropriately scaled to normalize the total source power with respect to this elementary source. In this way, it is possible to account for the effects of the PSF of the microphone array [see Fig. 2(b)]. Therefore, the resulting sound power P is expressed by

$$P = \frac{\sum_{j\in\mathrm{ROI}} \boldsymbol{w}_j^*\,\boldsymbol{C}\,\boldsymbol{w}_j}{\sum_{j\in\mathrm{ROI}} \boldsymbol{w}_j^*\left(\boldsymbol{g}_j\,\boldsymbol{g}_j^*\right)\boldsymbol{w}_j}. \tag{9}$$

In this work, the scan grid for evaluating the potential sources is planar and parallel to the microphone-array distribution. It is 1 × 1 m wide, features a spatial resolution of 0.01 m, and, for each chunk, is centered at the position of the drone provided by the motion capture system. The ROI has its center at the same location and extends over an area of 0.5 × 0.5 m. In this way, it encompasses the total sound source and is large enough to capture the potential main-lobe broadening due to coherence loss while excluding the contribution of side lobes in the sound map (Merino-Martínez *et al.*, 2019). Finally, the integrated

power spectra are computed for a frequency range of 0.1–5 kHz, which represents the range of validity of the method of images in the derived tailored Green's function (see Sec. II B).

The last step of the proposed methodology to investigate maneuvering drone noise is the transition of the integrated power spectra back to the time domain. This is done by backpropagating the amplitude of the decontaminated acoustic pressure p' at the receiver location for each chunk and frequency, which reads

$$p'(\boldsymbol{x}_r, f) = \frac{P^{0.5}}{4\pi||\boldsymbol{x}_r - \boldsymbol{x}_s||}. \tag{10}$$

Here, the vector norm $||\boldsymbol{x}_r - \boldsymbol{x}_s||$ represents the distance between the tracked position of the drone and the central microphone of the array. Equation (10) refers to a source radiating in free-field conditions, i.e., with spherical spreading. Different amplitude corrections can be implemented to include reverberation effects, as will be discussed in Sec. III A. p' is then reconstructed as a time signal using the Griffin–Lim algorithm (Griffin and Lim, 1984), which is a phase reconstruction method based on the redundancy of the short-time Fourier transform that promotes the consistency of the spectrogram using a gradient descent approach (Ji and Tie, 2016). This procedure allows, for instance, psychoacoustic assessments to be conducted on the signal decontaminated by reverberation effects.

III. RESULTS AND DISCUSSION

A. Acoustic characterization of the test hall

This section presents the results of the acoustic characterization of the ID2Move test hall with the goal of validating the tailored Green's function approach proposed to decontaminate the signal from reverberation effects. Specifically, the first part focuses on assessing the influence of constructive and destructive interference on the acoustic field, while the second investigates the sound decay inside the test hall. A preliminary version of these results has recently been presented by Zamponi *et al.* (2024).

Figure 5 displays the TF [see Eq. (6)] between the test hall, i.e., in reverberant conditions, and the VKI anechoic chamber, i.e., in free-field conditions, obtained from the experimental measurements and predicted analytically. The latter calculation is performed using the method of images for both a rectangular room resembling the ID2Move facility and a hemi-anechoic environment where only the sound reflected by the floor is considered. Two different monopolar source heights are investigated, while the location of the microphone is kept constant (see Sec. II A). The results demonstrate that the effects of sound reflections in the test hall are non-negligible. Specifically, compared to anechoic conditions, the experimental TF exhibits constructive/destructive interference patterns induced by sound reflections, with deviations on the order of ± 5 dB. Furthermore, the analytical prediction shows reasonably good agreement with the measurements across the considered frequency range. This outcome suggests that the method of images is suitable for calculating the acoustic field in the test hall, even though the room is not exactly rectangular and other objects present in the experimental setup are not accounted for in the model (Zamponi *et al.*, 2024). Interestingly, the computation obtained considering only the floor reflections correctly predicts the experimental trend and suggests that the floor is primarily responsible for the interference effects seen in the microphone recordings, provided that the source is sufficiently far from the ceiling and side walls and within the reverberation radius of the room D_c.

The analytical TF derived above can now be used to correct the spectra of the signal acquired in the room. This procedure aims to account for the influence of sound reflections on the sound pressure levels obtained in reverberant conditions. The correction is tested in measurements carried out with the monopolar source in the test hall and the L_p variations between the microphone signal at 0.1 m and that at

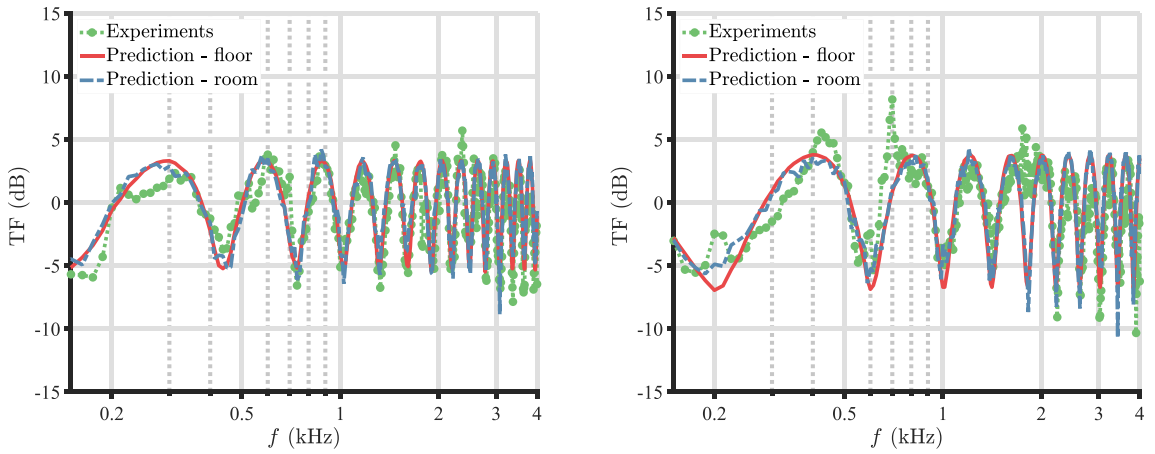

FIG. 5. Transfer function (TF) [see Eq. (6)] between free-field conditions measured in the anechoic chamber and the ID2Move test hall. The microphone is placed at a height of 1 m and a distance of 1 m from the monopolar source (see Sec. II A), whose height is set to (A) 0.9 m and (B) 0.6 m.

https://doi.org/10.1121/10.0036900

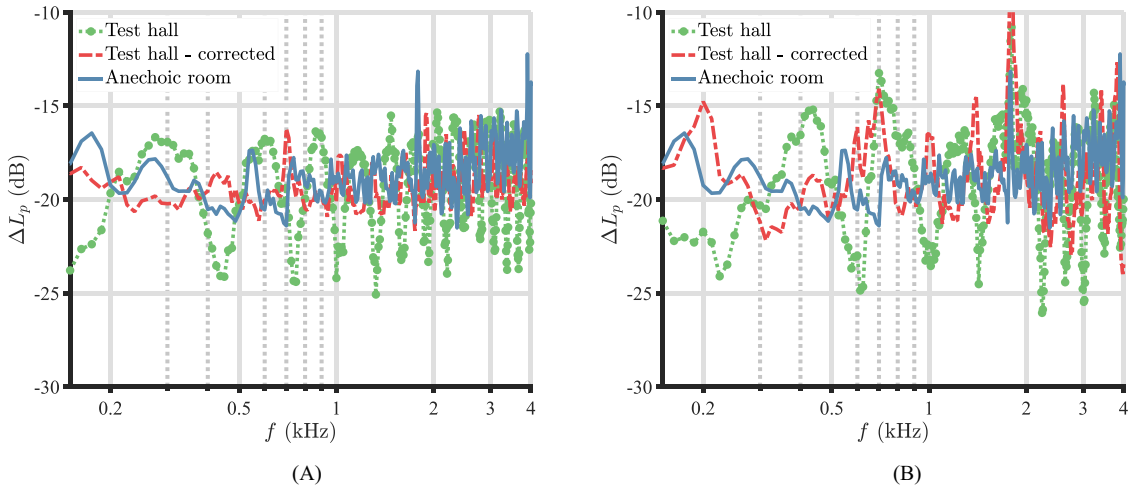

FIG. 6. Variation in sound pressure level between the microphone signals at 0.1 and 1 m, measured under anechoic conditions, in the test hall, and in the test hall with TF correction applied. The monopolar source height is set to (A) 0.9 m and (B) 0.6 m.

1 m for the different source heights are presented in Fig. 6. As mentioned in Sec. II A, expressing the sound pressure levels relative to the near-field microphone compensates for the varying amplitudes of the loudspeaker driving the monopolar source in the anechoic chamber and the test hall, making the comparison more robust. The analysis demonstrates that the corrected spectra effectively eliminate the oscillating trend caused by interference effects from ground reflections (Zamponi *et al.*, 2024), although minor deviations remain, particularly in the low-frequency range and when the source is closer to the floor. These discrepancies reflect those observed in the TF in Fig. 5 and may be due to minor deviations of the interpolated absorption coefficients from the realistic conditions (see the Appendix). However, since the drone is typically flown at altitudes higher than 1 m, this is not expected to impact the conclusions drawn in the following analysis, although potential inaccuracies may still arise if the methodology is applied during takeoff or landing operations, or in the case of large drones exhibiting lower blade passing frequencies.

To assess the influence of reverberation on sound decay, the acoustic field induced by the monopolar source in the test hall is calculated using the method of images and compared with the measurements of the microphone at various distances from the loudspeaker. The results of this study, which illustrate how the sound pressure level L_p changes over the distance in the room, are presented in Fig. 7. The effect of reverberation is evident by the fact that the sound does not decay following the inverse square law, which is valid under free-field conditions and states that the acoustic pressure is inversely proportional to the distance (Glegg and Devenport, 2017), but rather at a lower rate. This outcome is expected, considering that the acoustic power is constrained inside the room as a result of the acoustic reflections. Upon comparing the analytical computations with the experimental results, the decay law predicted by the method of images, which can be approximated by a power law with an exponent of –0.5 (characteristic of cylindrical spreading), well represents the sound-decay trend in the room within a range of 5 m, exhibiting maximum deviations within 1 dB (Zamponi *et al.*, 2024). In this case, accounting for only the sound reflection by the floor is not sufficient to achieve a satisfactory prediction, implying that the tailored Green's function for a rectangular room is required to model the acoustic response of the ID2Move test hall.

The considerations made above for the sound decay being proportional to a power law with an exponent of –0.5 as a consequence of the tailored Green's function of the test hall also apply to the backpropagation of the acoustic pressure in Eq. (10), which now reads

$$p'(\boldsymbol{x}_r, f) = \frac{P^{0.5}}{4\pi||\boldsymbol{x}_{r=1\mathrm{m}} - \boldsymbol{x}_s||} \left(\frac{||\boldsymbol{x}_{r=1\mathrm{m}} - \boldsymbol{x}_s||}{||\boldsymbol{x}_r - \boldsymbol{x}_s||}\right)^{0.5}, \quad (11)$$

with $\boldsymbol{x}_{r=1\mathrm{m}}$ being the coordinates of a reference receiver placed at 1 m of distance from the source. In order to

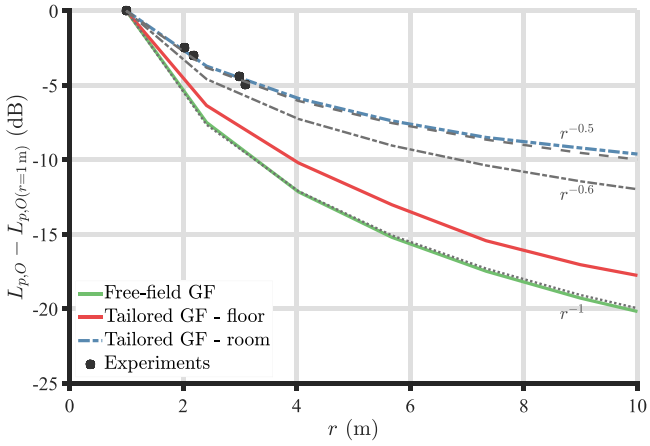

FIG. 7. Overall-sound-pressure-level decay over the distance computed using the method of images. $L_{p,O}$ is normalized using the value recorded at 1 m of distance. The simulation is performed in a rectangular room with the same dimensions as the ID2Move test hall and a monopolar source at the position $x = 6$ m, $y = 6$ m, and $z = 1.5$ m.

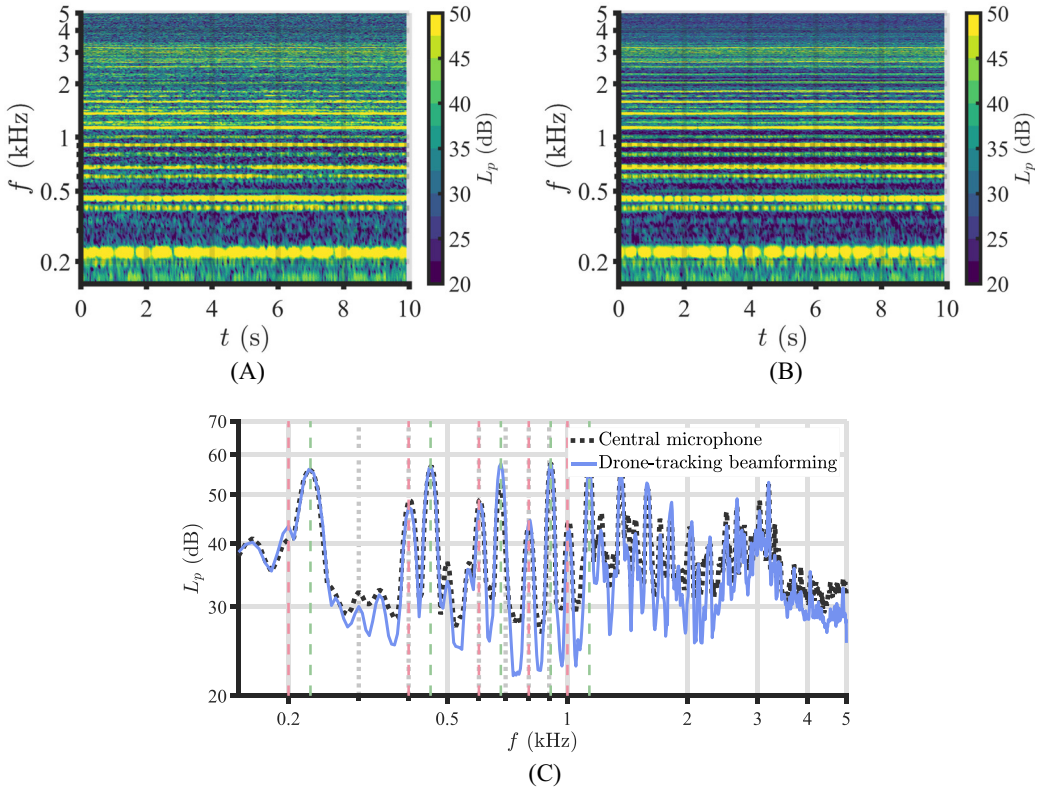

FIG. 8. Spectrograms measured by the (A) central microphone and (B) reconstructed by drone-tracking beamforming for a drone hovering at 1 m from the array and at a height of 1.3 m. (C) Time-averaged sound pressure levels, where the two BPFs and their harmonics are highlighted up to the fourth harmonic. The data are computed with a reference pressure of $p_{\text{ref}} = 20\,\mu$Pa.

compare the noise radiated by different operations in the results discussed in the subsequent analysis, the distance between the minimum tracked position of the drone during each maneuver ($\boldsymbol{x}_s$) and the central microphone of the array ($\boldsymbol{x}_r$) is normalized at a reference value of 2 m.

B. Assessment of the dereverberation effect

The impact of the decontamination from reverberation effects in the test hall on drone acoustics is now assessed by comparing the signal acquired by the central microphone of the array with that reconstructed through the beamforming method. The comparison is carried out for the UAV in hovering conditions, which is presented here as a validation test case. The sound pressure levels and spectrograms for a hovering drone at 1 m distance from the array and approximately aligned with its center, i.e., at a height of 1.3 m, are reported in Fig. 8.

As expected, the acoustic footprint of the UAV is dominated by the tonal component of the frequency spectrum, especially at low frequencies, whereas the broadband part is more significant at high frequencies, with a maximum around 3 kHz that may be linked to electric motor noise (Huff and Henderson, 2018). The narrow noise peaks are located at frequencies that are the exact multiple of two close yet distinguished blade pass frequencies (BPFs), as highlighted in Fig. 8. This outcome is explained by the fact that the front propellers spin at a different rotational speed than the back ones, owing to the asymmetrical architecture of the DJI Air 2S (see Sec. II). The spectrograms also show that the BPFs are constant in time, demonstrating the stability of such a drone model in hovering conditions and the negligible influence of flow recirculation in the test hall. However, the amplitudes of the tonal peaks exhibit a modulation that is most likely associated with an adjustment of the propeller speeds by the UAV controller.

The main effect of dereverberation is to decrease the radiated broadband noise levels for $f > 0.5$ kHz and increase the dynamic range of the BPF peaks, which can be visualized more clearly in the spectrogram. In other words, drone-tracking beamforming facilitates tracking the tonal components of the frequency spectrum, and this proves particularly beneficial for aeroacoustic investigation of the UAV during maneuvering conditions. Furthermore, part of these peaks is amplified, and part is attenuated as a consequence of the interference pattern caused by sound reflections (see Fig. 5). The method additionally enables a clearer visualization of the modulation of the peak amplitudes at the BPFs due to the controller.

If the drone hovers at a higher altitude, i.e., 2 m, the influence of the test hall floor becomes less important, as Fig. 9 shows. In this case, the signal acquired by the central microphone and that reconstructed by the proposed methodology provide comparable L_p contributions, since the conditions experienced by the UAV are closer to those in the free field. Hence, it is reasonable to expect that the impact of the dereverberation varies during the drone maneuver depending on its distance from reflective surfaces. The

https://doi.org/10.1121/10.0036900

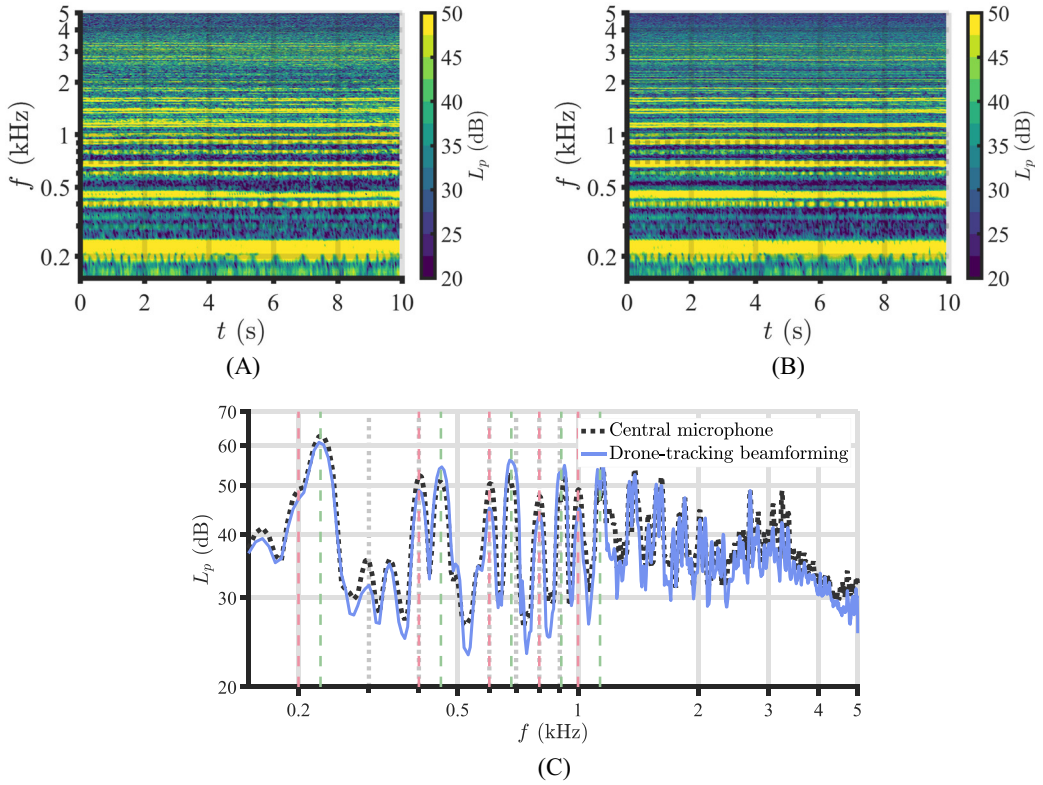

FIG. 9. Spectrograms measured by the (A) central microphone and (B) reconstructed by drone-tracking beamforming for a drone hovering at 1 m from the array and at a height of 2 m. (C) Time-averaged sound pressure levels, where the two BPFs and their harmonics are highlighted up to the fourth harmonic. The data are computed with a reference pressure of $p_{\text{ref}} = 20\,\mu$Pa.

agreement between the acquired and reconstructed sound pressure levels also corroborates the validity of the scaling law in Eq. (11) in modeling the sound decay in the test hall.

It is important to mention that, for a formal validation of the dereverberation methodology, the UAV noise radiated in the test hall should be directly compared with that emitted in the free field under the same conditions. However, making such a comparison would be challenging due to the flight controller of the drone. On the one hand, outdoor measurements would be hindered by uncontrolled atmospheric disturbances, which would require continuous stabilization of the propeller speeds, as mentioned in Sec. I. On the other hand, the VKI anechoic room is a confined space where the drone wake is likely to be reinjected into the propellers, altering its stability. These changes in propeller speed produced by the controller would likely affect drone noise, preventing validation. Therefore, a different experimental procedure would be necessary for this comparison. Although not fully representative of drone operation, one possible solution could be to perform fixed-rotor measurements with a prescribed propeller speed. This will be a topic for future work.

C. Investigation of the maneuvering drone

In this section, the noise emitted by the drone during the maneuvers listed in Fig. 4 and reconstructed using the drone-tracking beamforming is investigated. A total of three measurements were performed for each maneuver to verify the repeatability of the results. Each of the spectrograms reported in the following is complemented by a graph that shows the evolution of the drone relative position with respect to the center of the array (vector $\boldsymbol{d}$) and velocity (vector $\boldsymbol{v}$) over time, allowing interpretation of the acoustic data in function of the UAV dynamics.

Before discussing the acoustic footprint of the different maneuvers, it is important to analyze the noise emission deviations that occur when the drone faces the receiver—during side-to-side and vertical flights—or is oriented sideways relative to the receiver—during side-to-side and forward flights. In Fig. 10, the sound pressure levels from

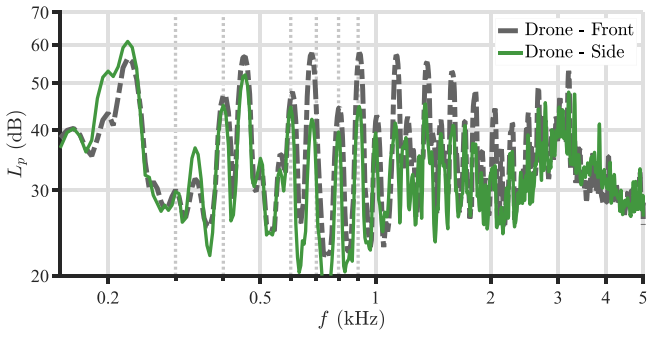

FIG. 10. Sound pressure levels reconstructed by drone-tracking beamforming for a drone facing the array (dashed-dotted line) and oriented sideways (solid line). The UAV hovers at 1 m from the array and at a height of 1.3 m. The data are computed with a reference pressure of $p_{\text{ref}} = 20\,\mu$Pa.

Fig. 8(C) are compared to those produced by the drone hovering at the same position (1 m from the array and at a height of 1.3 m) but oriented sideways. Interestingly, a substantial reduction in the amplitude of the harmonics of the highest BPF up to 15 dB is observed in the latter case, whereas the broadband noise region around 3 kHz appears to be mostly unaltered by the orientation of the UAV. This result is supported by the fact that the front rotors spin at a higher speed in order to maintain vehicle stability, and when the drone is oriented sideways, one of them is partially shielded, mitigating the amplitude of the peak for this BPF and the related harmonics.

The spectrogram associated with the drone accelerating in forward flight is presented in Fig. 11. The data are additionally plotted against the frequency normalized by the BPF of the front rotors of the hovering drone to better visualize the evolution of the propeller speed over time. In this case, the amplitudes of the tonal contributions are consistent with the hover of the drone oriented sideways. The difference in rotational speed between the front and back rotors appears to be reduced when the UAV is operated in forward flight. This effect is probably due to the change in the drone pitch, which results in an adjustment in the rotor speeds, and is more accentuated at higher velocities. As a result, the two BPFs and related harmonics tend to converge during the maneuver and almost overlap by the end of it. Moreover, the broadband noise around 3 kHz appears to increase with increasing v_x, which may be connected with the ingestion of more disturbed inflow by the aft rotors.

Similar explanations can be speculated on when the drone decelerates in forward flight (Fig. 12). In this case, the BPFs and their harmonics tend to diverge over time from approximately 0.16 s on, although the tonal contributions are less clearly separated at the beginning of the deceleration phase. Likewise, broadband noise decreases along with drone speed.

The scenario pictured above is confirmed when the drone is operated side-to-side, which is presented in Fig. 13.

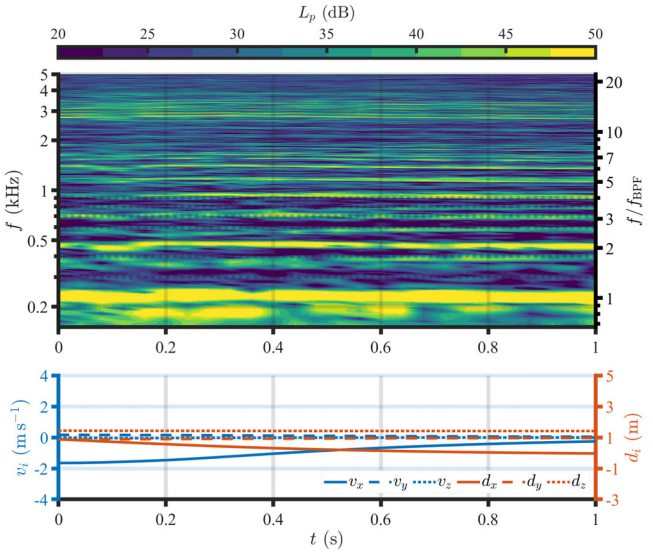

FIG. 12. On the top, the spectrogram reconstructed by drone-tracking beamforming referred to a drone decelerating in forward flight [Fig. 4(B)]. The data are computed with a reference pressure of $p_{\mathrm{ref}} = 20\,\mu$Pa. On the right axis, the frequency is normalized by the BPF associated with the front rotors of the hovering drone. On the bottom, the trajectory followed by the drone and evolution of the vector components describing its velocity ($\boldsymbol{v}$) and relative position ($\boldsymbol{d}$) with respect to the array center.

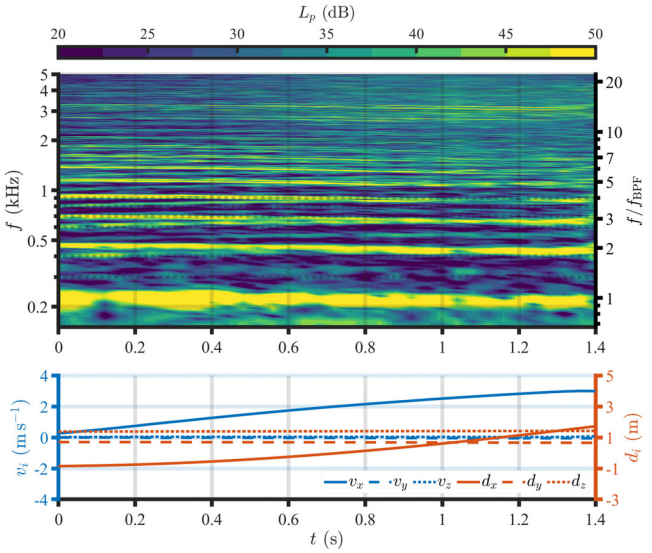

FIG. 11. On the top, the spectrogram reconstructed by drone-tracking beamforming referred to a drone accelerating in forward flight [Fig. 4(A)]. The data are computed with a reference pressure of $p_{\mathrm{ref}} = 20\,\mu$Pa. On the right axis, the frequency is normalized by the BPF associated with the front rotors of the hovering drone. On the bottom, the trajectory followed by the drone and evolution of the vector components describing its velocity ($\boldsymbol{v}$) and relative position ($\boldsymbol{d}$) with respect to the array center.

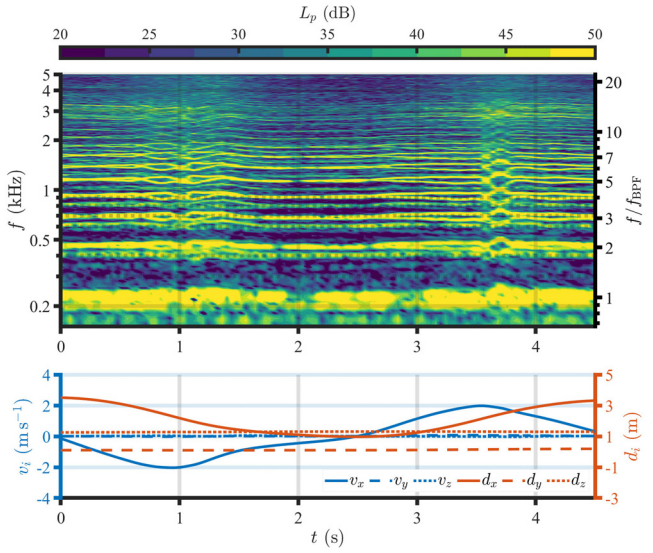

FIG. 13. On the top, the spectrogram reconstructed by drone-tracking beamforming referred to a drone moving side-to-side [Fig. 4(C)]. The data are computed with a reference pressure of $p_{\mathrm{ref}} = 20\,\mu$Pa. On the right axis, the frequency is normalized by the BPF associated with the front rotors of the hovering drone. On the bottom, the trajectory followed by the drone and evolution of the vector components describing its velocity ($\boldsymbol{v}$) and relative position ($\boldsymbol{d}$) with respect to the array center.

https://doi.org/10.1121/10.0036900

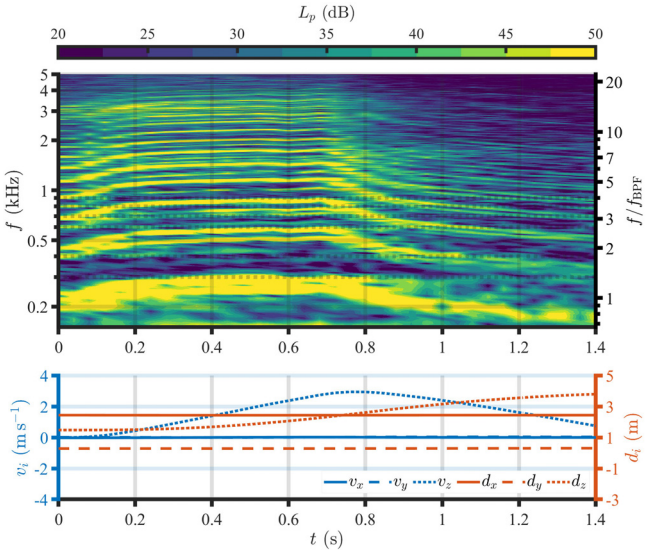

FIG. 14. On the top, the spectrogram reconstructed by drone-tracking beamforming referred to a drone ascending in vertical flight [Fig. 4(D)]. The data are computed with a reference pressure of $p_{ref} = 20\,\mu$Pa. On the right axis, the frequency is normalized by the BPF associated with the front rotors of the hovering drone. On the bottom, the trajectory followed by the drone and evolution of the vector components describing its velocity ($\boldsymbol{v}$) and relative position ($\boldsymbol{d}$) with respect to the array center.

The fact that the drone faces the array during this maneuver results in higher amplitudes of tonal contributions compared to previous forward flights, consistent with the analysis of Fig. 10. The acceleration and deceleration phases of the maneuver are associated with BPFs that get closer and farther away, respectively. In particular, the largest tone splitting is observed in correspondence with changes in the drone direction, occurring at $t \approx 1.1$ s and $t \approx 3.6$ s. These results, which could not be achieved without effective decontamination from the reverberation effects, further confirm the key role that the information provided by the motion capture system plays in interpreting the noise emitted by the UAV.

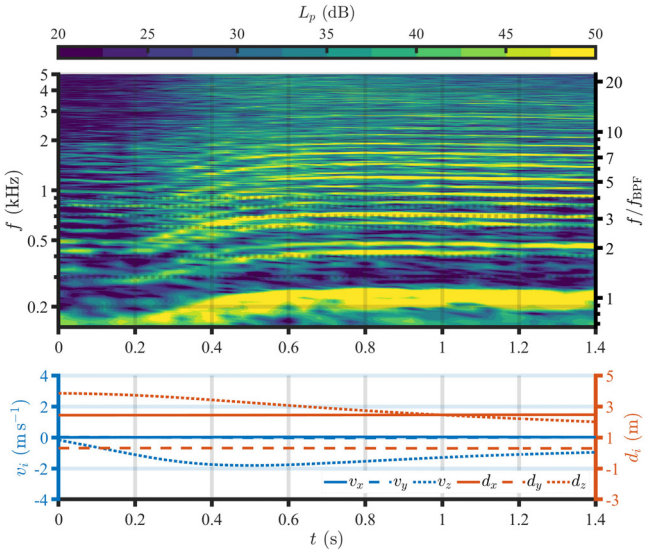

FIG. 15. On the top, the spectrogram reconstructed by drone-tracking beamforming referred to a drone descending in vertical flight [Fig. 4(E)]. The data are computed with a reference pressure of $p_{ref} = 20\,\mu$Pa. On the right axis, the frequency is normalized by the BPF associated with the front rotors of the hovering drone. On the bottom, the trajectory followed by the drone and evolution of the vector components describing its velocity ($\boldsymbol{v}$) and relative position ($\boldsymbol{d}$) with respect to the array center.

When the drone is operated in vertical flight, the relative differences in front and back rotor speeds observed in hovering conditions do not vary since the pitch remains unchanged. During the ascent (Fig. 14), the propellers spin at a higher rotational speed, resulting in an increase in BPF. The spectra suddenly change at $t \approx 0.75$ s, when the rotors decelerate, causing a steep decrease in the BPF, and the drone starts stabilizing at a constant altitude. The same considerations apply to the UAV descending in vertical flight (Fig. 15). In this case, the drone significantly reduces the rotational speed of the propellers to decrease the altitude. Afterward, it increases the rotor speeds to $t \approx 0.6$ s in order to gradually counterbalance the effect of gravity and promote stabilization at a constant altitude. Above this threshold, the propeller speeds do not change, and they adjust to those observed for the hover in Fig. 8.

IV. CONCLUSIONS

This research aims to present an experimental methodology for accurately investigating the noise radiated by a maneuvering UAV in a reverberant environment, as an alternative to anechoic environments and open-field tests. Measurements of a commercial quadcopter drone have been carried out in the ID2Move test hall, which offers a spacious environment in which the UAV trajectory can be accurately tracked with a state-of-the-art motion capture system. The facility has been acoustically characterized by means of simplified monopolar sources to understand the influence of sound reflections on the drone noise measurements. The results show that reverberation effects in the test hall cannot be ignored and cause variations in the measured sound pressure level of up to ± 5 dB with respect to anechoic conditions. For a receiver placed within the critical distance from the source, the constructive/destructive interference pattern induced by sound reflections is primarily due to the presence of the floor. In addition, the sound decay in the room is found to be proportional to a power law with an exponent of -0.5, consistent with cylindrical spreading. The outcome of this characterization allows the tailored Green's function of the test hall associated with a monopolar source and, hence, its acoustic response to be analytically derived.

A novel method that combines a phased-array technique with the reconstruction of the drone trajectory is proposed to decontaminate the radiated noise from the reverberation effects. The time signal recorded by the microphone array is divided into short chunks, and a sound map centered on the tracked location of the drone is reconstructed for each chunk. The assumption that the scan grid of potential sound sources consists of uncorrelated monopoles makes it possible to apply the aforementioned tailored Green's function in

the steering-vector formulation. Afterward, the sound maps are integrated within a pre-defined ROI to estimate the source power related to the chunk. This approach additionally enables phase reconstruction of the integrated source power using the Griffin–Lim algorithm, which will be exploited in future investigations to evaluate the PA of the drone in the time domain. The proposed methodology is initially assessed in the case of the drone in hovering conditions, showing that the impact of the decontamination from the reverberation effects is more significant the closer to the ground the drone is operated, and subsequently applied to several maneuvers, including forward and vertical flights.

The aeroacoustic results show that the tonal contributions of the noise spectrum are heavily affected by the UAV operation and orientation. When the drone is oriented sideways instead of facing the microphone array, a substantial reduction of up to 15 dB is observed in the harmonics of the highest BPF, which is associated with the front rotors of the hovering drone. This result suggests the presence of a complex directivity pattern influenced by the architecture of the UAV and the location of the motors. Moreover, the two distinct BPFs that characterize the drone in hover due to the imbalance between the front and back motors get closer and farther during the acceleration and deceleration phases in the forward flights, respectively. This is probably due to adjustments in propeller rotational speeds in response to a modification in pitch to maintain drone stability within the maneuver. The same does not occur for vertical flight, as the UAV maintains a horizontal position. These results demonstrate the crucial role that drone trajectory information plays in investigating related noise emissions.

In conclusion, the proposed decontamination methodology enables accurate acoustic measurements in a reverberant environment, taking full advantage of the controlled atmospheric conditions that characterize the test hall and the motion capture system with which it is equipped. This approach will make it possible to generate extensive datasets of well-documented drone maneuvers in the ID2Move facility, which can offer the opportunity to improve the current understanding of drone maneuvering noise and foster further research on innovative strategies to reduce its annoyance for humans.

ACKNOWLEDGMENTS

The authors thank Emilien Watelet for access to the ID2Move facility and support during the measurement campaigns. The research presented in this paper has been funded by the European Union's Horizon Europe Research and Innovation program under Grant No. 101138209 (eVTOLUTION). Views and opinions expressed are, however, those of the authors only and do not necessarily reflect those of the European Union or the European Climate, Infrastructure and Environment Executive Agency (CINEA). Neither the European Union nor the granting authority can be held responsible for them.

TABLE I. Table of reflection coefficients for the floor and walls of the ID2Move test hall.

f (kHz)	0.125	0.25	0.5	1	2	4
β_{floor}	0.98	0.98	0.97	0.97	0.96	0.95
β_{wall}	0.94	0.95	0.98	0.99	0.98	1.00

AUTHOR DECLARATIONS

Conflict of Interest

The authors have no conflicts to disclose.

DATA AVAILABILITY

Data supporting the findings of this study are available from the corresponding author upon reasonable request.

APPENDIX: WALL-REFLECTION COEFFICIENTS

The frequency-dependent absorption coefficients of the test hall are determined considering the material specifications of its walls and floor (Vaverka *et al.*, 1998). In particular, the former are made of plasterboard, whereas the latter are made of vinyl. The reflection coefficients β_a are then calculated from Eq. (5). The results are listed in Table I for discrete frequencies ranging from 125 Hz to 4 kHz. Elsewhere, β_a has been interpolated.

Alkmim, M., Cardenuto, J., Tengan, E., Dietzen, T., Van Waterschoot, T., Cuenca, J., De Ryck, L., and Desmet, W. (**2022**). "Drone noise directivity and psychoacoustic evaluation using a hemispherical microphone array," J. Acoust. Soc. Am. **152**(5), 2735–2745.

Allen, C. S., Blake, W. K., Dougherty, R. P., Lynch, D., Soderman, P. T., and Underbrink, J. R. (**2002**). *Aeroacoustic Measurements* (Springer, Berlin Heidelberg).

Allen, J. B., and Berkley, D. A. (**1979**). "Image method for efficiently simulating small-room acoustics," J. Acoust. Soc. Am. **65**(4), 943–950.

Amoiridis, O., Zarri, A., Zamponi, R., Pasco, Y., Yakhina, G., Christophe, J., Moreau, S., and Schram, C. (**2022**). "Sound localization and quantification analysis of an automotive engine cooling module," J. Sound Vib. **517**, 116534.

Aretz, M., Dietrich, P., and Vorländer, M. (**2014**). "Application of the mirror source method for low frequency sound prediction in rectangular rooms," Acta Acust. united Acust. **100**(2), 306–319.

Blanchard, T., Thomas, J.-H., and Raoof, K. (**2020**). "Acoustic localization and tracking of a multi-rotor unmanned aerial vehicle using an array with few microphones," J. Acoust. Soc. Am. **148**(3), 1456–1467.

Cavanaugh, W. J., Tocci, G. C., and Wilkes, J. A. (**2010**). *Architectural Acoustics: Principles and Practice*, 2nd ed. (John Wiley & Sons, Hoboken, NJ).

Davis, D., Patronis, E., Brown, P., and Ballou, G. (**2013**). *Sound System Engineering*, 4th ed. (Focal Press, Burlington, MA).

Dougherty, R. P. (**1998**). "Spiral-shaped array broadband imaging," U.S. patent 5,838,284.

Falorca, J. F., Miraldes, J. P. N. D., and Lanzinha, J. C. G. (**2021**). "New trends in visual inspection of buildings and structures: Study for the use of drones," Open Eng. **11**(1), 734–743.

Gallo, E., Beaulieu, G., and Schram, C. F. (**2022**). "Annoyance factors of a maneuvering multicopter drone," in *28th AIAA/CEAS Aeroacoustics 2022 Conference*, American Institute of Aeronautics and Astronautics, Southampton, UK.

Glegg, S. A. L., and Devenport, W. (**2017**). *Aeroacoustics of Low Mach Number Flows: Fundamentals, Analysis, and Measurement* (Academic Press, London, UK).

Green, N., Torija, A. J., and Ramos-Romero, C. (**2024**). "Perception of noise from unmanned aircraft systems: Efficacy of metrics for indoor and outdoor listener positions," J. Acoust. Soc. Am. **155**(2), 915–929.

Griffin, D. W., and Lim, J. S. (**1984**). "Signal estimation from modified short-time Fourier transform," IEEE Trans. Acoust. Speech Signal Process. **32**, 236–469.
Guo, J., Ahmad, I., and Chang, K. (**2020**). "Classification, positioning, and tracking of drones by HMM using acoustic circular microphone array beamforming," J. Wireless Com Network **2020**, 9.
Gupta, A., Afrin, T., Scully, E., and Yodo, N. (**2021**). "Advances of UAVs toward future transportation: The state-of-the-art, challenges, and opportunities," Future Transp. **1**(2), 326–350.
Gwak, D. Y., Han, D., and Lee, S. (**2020**). "Sound quality factors influencing annoyance from hovering UAV," J. Sound Vib. **489**, 115651.
Herold, G., and Sarradj, E. (**2023**). "Microphone array based trajectory reconstruction for small UAV fly-by measurements," in *AIAA AVIATION 2023 Forum*, American Institute of Aeronautics and Astronautics, San Diego, CA and Online.
Herold, G., and Sarradj, E. (**2024**). "Characterizing multicopter UAV noise emission through outdoor fly-by measurements with a microphone array," in *30th AIAA/CEAS Aeroacoustics Conference (2024)*, American Institute of Aeronautics and Astronautics, Rome, Italy.
Huff, D. L., and Henderson, B. S. (**2018**). "Electric motor noise for small quadcopters: Part 1 – acoustic measurements," in *2018 AIAA/CEAS Aeroacoustics Conference*, American Institute of Aeronautics and Astronautics, Atlanta, GA.
ID2Move (**2025**). https://www.id2move.eu/our-services/test-range (Last viewed May 15, 2025).
Intaratep, N., Alexander, W. N., Devenport, W. J., Grace, S. M., and Dropkin, A. (**2016**). "Experimental study of quadcopter acoustics and performance at static thrust conditions," in *22nd AIAA/CEAS Aeroacoustics Conference*, American Institute of Aeronautics and Astronautics, Lyon, France.
ISO 5305:2024, (**2024**). "Noise measurements UAS (unmanned aircraft systems)" (International Organization for Standardization, Geneva, Switzerland).
Ji, L., and Tie, Z. (**2016**). "On gradient descent algorithm for generalized phase retrieval problem," in *2016 IEEE 13th International Conference on Signal Processing (ICSP)*, IEEE, Chengdu, China, pp. 320–325.
Kellermann, R., Biehle, T., and Fischer, L. (**2020**). "Drones for parcel and passenger transportation: A literature review," Transp. Res. Interdiscip. Perspect. **4**, 100088.
Kim, D. H., Park, C. H., and Moon, Y. J. (**2019**). "Aerodynamic analyses on the steady and unsteady loading-noise sources of drone propellers," Int. J. Aeronaut. Space Sci. **20**(3), 611–619.
Merino-Martínez, R., Luesutthiviboon, S., Zamponi, R., Rubio Carpio, A., Ragni, D., Sijtsma, P., Snellen, M., and Schram, C. (**2020**). "Assessment of the accuracy of microphone array methods for aeroacoustic measurements," J. Sound Vib. **470**, 115176.
Merino-Martínez, R., Sijtsma, P., Rubio Carpio, A., Zamponi, R., Luesutthiviboon, S., Malgoezar, A., Snellen, M., Schram, C., and Simons, D. (**2019**). "Integration methods for distributed sound sources," Int. J. Aeroacoust. **18**(4-5), 444–469.
Moriaux, O., Zamponi, R., and Schram, C. (**2024**). "Semi-empirical calibration of remote microphone probes using Bayesian inference," J. Sound Vib. **573**, 118197.
Naz, P., Hengy, S., Ramamonjy, A., Rassy, O., and Bavu, E. (**2020**). "Outdoor field trials for the measurement of the acoustic signals of mini UAVs," in *e-Forum Acusticum 2020*, Lyon, France (virtual), pp. 3155–3162.
Poozesh, P., Aizawa, K., Niezrecki, C., Baqersad, J., Inalpolat, M., and Heilmann, G. (**2017**). "Structural health monitoring of wind turbine blades using acoustic microphone array," Struct. Health Monit **16**(4), 471–485.
Ramos-Romero, C., Green, N., Torija, A. J., and Asensio, C. (**2023**). "On-field noise measurements and acoustic characterisation of multi-rotor small unmanned aerial systems," Aerosp. Sci. Technol. **141**, 108537.
Rizzi, S. A., Huff, D. L., Boyd, D. D., Bent, P., Henderson, B. S., Pascioni, K. A., Sargent, D. C., Josephson, D. L., Marsan, M., He, H. B., and Snider, R. (**2020**). "Urban Air Mobility Noise: Current Practice, Gaps, and Recommendations," Technical Report, National Aeronautics and Space Administration, Langley Research Center, Hampton, VA.
Roger, M., and Moreau, S. (**2020**). "Tonal-noise assessment of quadrotor-type UAV using source-mode expansions," Acoustics **2**(3), 674–690.
Sabatini, R., and Gardi, A. (**2023**). *Sustainable Aviation Technology and Operations: Research and Innovation Perspectives*, 1st ed. (Wiley, Hoboken, NJ).
Sarikaya, B., Zarri, A., Christophe, J., Aissa, M. H., Verstraete, T., and Schram, C. (**2024**). "Aerodynamic and aeroacoustic design optimization of UAVs using a surrogate model," J. Sound Vib. **589**, 118539.
Savioja, L., and Svensson, U. P. (**2015**). "Overview of geometrical room acoustic modeling techniques," J. Acoust. Soc. Am. **138**(2), 708–730.
Scalea, J. R., Restaino, S., Scassero, M., Blankenship, G., Bartlett, S. T., and Wereley, N. (**2018**). "An initial investigation of unmanned aircraft systems (UAS) and real-time organ status measurement for transporting human organs," IEEE J. Transl. Eng. Health Med. **6**, 4000107.
Schäffer, B., Pieren, R., Heutschi, K., Wunderli, J. M., and Becker, S. (**2021**). "Drone noise emission characteristics and noise effects on humans—A systematic review," Int. J. Environ. Res. Public Health **18**(11), 5940.
Shafiee, M., Zhou, Z., Mei, L., Dinmohammadi, F., Karama, J., and Flynn, D. (**2021**). "Unmanned aerial drones for inspection of offshore wind turbines: A mission-critical failure analysis," Robot **10**(1), 26.
Torija, A. J., and Nicholls, R. K. (**2022**). "Investigation of metrics for assessing human response to drone noise," Int. J. Environ. Res. Public Health **19**(6), 3152.
Torija, A. J., Self, R. H., and Lawrence, J. L. (**2019**). "Psychoacoustic characterisation of a small fixed-pitch quadcopter," in *Inter-Noise and Noise-Con Congress and Conference Proceedings, Institute of Noise Control Engineering* [Spanish Acoustical Society (SEA), Madrid, Spain], Vol. 259, pp. 1884–1894.
Torija, A. J., Ramos-Romero, C. A., and Green, N. (**2024**). "Acoustic and psychoacoustic characterisation of unmanned aircraft systems as a function of vehicle mass and flight procedure," in *30th AIAA/CEAS Aeroacoustics Conference (2024)*, American Institute of Aeronautics and Astronautics, Rome, Italy.
Vaverka, J., Kozel, V., Ládyš, L., Liberko, M., and Chybík, J. (**1998**). *Stavební Fyzika I. Urbanistická, Stavební a Prostorová Akustika (Building Physics I. Urban Planning, Building and Space Acoustics)* (VUTIUM, Brno, Czech Republic).
Waterhouse, R. V. (**1958**). "Output of a sound source in a reverberation chamber and other reflecting environments," J. Acoust. Soc. Am. **30**(1), 4–13.
Welch, P. (**1967**). "The use of fast Fourier transform for the estimation of power spectra: A method based on time averaging over short, modified periodograms," IEEE Trans. Audio Electroacoust. **15**(2), 70–73.
Whelchel, J., Alexander, W. N., Pisharoti, N., Brizzolara, S., Murali, R., and Stilwell, D. (**2022**). "Examination of broadband and tonal noise sources produced by eVTOL propellers and drive systems," in *28th AIAA/CEAS Aeroacoustics 2022 Conference*, American Institute of Aeronautics and Astronautics, Southampton, UK.
Xu, Z., Herzog, A., Lodermeyer, A., Habets, E. A. P., and Prinn, A. G. (**2024**). "Simulating room transfer functions between transducers mounted on audio devices using a modified image source method," J. Acoust. Soc. Am. **155**(1), 343–357.
Yupa-Villanueva, R. M., Merino-Martinez, R., Altena, A., and Snellen, M. (**2024**). "Psychoacoustic characterization of multirotor drones in realistic flyover maneuvers," in *30th AIAA/CEAS Aeroacoustics Conference (2024)*, American Institute of Aeronautics and Astronautics, Rome, Italy.
Zamponi, R. (**2021**). "Investigation of turbulence-surface interaction noise mechanisms and their reduction using porous materials," Ph.D. thesis, Delft University of Technology, Delft, the Netherlands.
Zamponi, R., Gioli Torrione, G., Gallo, E., Zarri, A., Schillaci, L., and Schram, C. (**2024**). "Aeroacoustic assessment of the noise radiated by a maneuvering drone in an indoor test zone," in *30th AIAA/CEAS Aeroacoustics Conference (2024)*, American Institute of Aeronautics and Astronautics, Rome, Italy.
Zamponi, R., Satcunanathan, S., Moreau, S., Ragni, D., Meinke, M., Schröder, W., and Schram, C. (**2020**). "On the role of turbulence distortion on leading-edge noise reduction by means of porosity," J. Sound Vib. **485**, 115561.
Zamponi, R., Van de Wyer, N., and Schram, C. F. (**2019**). "Experimental investigation of airfoil turbulence-impingement noise reduction using porous treatment," in *25th AIAA/CEAS Aeroacoustics Conference*, American Institute of Aeronautics and Astronautics, Delft, The Netherlands.
Zarri, A., Dell'Erba, E., Munters, W., and Schram, C. (**2022**). "Aeroacoustic installation effects in multi-rotorcraft: Numerical investigations of a small-size drone model," Aerosp. Sci. Technol. **128**, 107762.
Zhou, T., Jiang, H., and Sun, X. (**2022**). "Noise source imaging measurements for small-scale multi-propeller systems," Appl. Acoust. **194**, 108801.